CEAS-GNC-2024-041

EuroGNC Navigation Guidance Control CEAS Bristol, UK June 11th-13th 2024
University of BRISTOL ROYAL AERONAUTICAL SOCIETY AIAA

Experimental Aided Inertial Estimation of Wing Shape for Flexible Aircraft Control

Rajashree Srikanth Graduate Student, ISAE-SUPAERO, Université de Toulouse, Toulouse, France. rajashree.srikanth@student.isae-supaero.fr

Inês M. G. S. Afonso Graduate Student, ISAE-SUPAERO, Université de Toulouse, Toulouse, France. ines.matias-gregorio-de-souza-afonso@student.isae-supaero.fr

Leandro R. Lustosa Associate Professor, ISAE-SUPAERO, Université de Toulouse, Toulouse, France. leandro.lustosa@isae-supaero.fr

ABSTRACT

This paper exhibits an instrumented flexible wing mockup demonstrating a wing shape estimation technique for automatic structural/flight control of very flexible aircraft undergoing large and geometrically nonlinear wing deflections. The proposed method exploits data fusion, using an extended Kalman filter, between distributed rate gyros across the wing and a sighting device at the wing root, and does not require knowledge of strain-displacement curves or specific aircraft dynamic models. The experiment is conducted in a motion capture room for ground truth availability and shows, as predicted in previous work, that the resulting estimation errors are bounded and have promising frequency response.

Keywords: Very Flexible Aircraft; Wing Shape Estimation; Kalman Filtering; Aeroelasticity.

1 Introduction

A current trend in aircraft design emphasizes lightweight aircraft combined with high-aspect-ratio wings for increased aerodynamic efficiency. The inherent flexibility in these modern designs interlaces structural dynamics with flight dynamics, traditionally treated separately, and calls for autopilot systems that account for the resulting aeroelastic coupling. Addressing these challenges, particularly for very flexible aircraft (VFA), demands innovative estimation techniques that capture the structural states of wings during flight in real time. Building upon previous theoretical work [1], this paper examines the viability of the method for wing shape estimation given real-world data for VFA control.

If a precise structural model of the aircraft is available, strain measurements can be translated to wing shape displacement estimates. For instance, Ref. [2] proposes using Fiber Bragg Gratings (FBG) strain measurements to compute wing shape deformation. In VFA flight mechanics models, wing shape determines aerodynamic behavior and is often preferred over strain variables. Additionally, strain measurements are subject to weather and require complex calibration techniques.

An alternative to strain measuring is to employ photogrammetric or stereo-vision techniques. References [3, 4] describe the significance of these measurements in understanding aircraft aerodynamics for moderately rigid aircraft (i.e., a Cessna Citation Sovereign and a Beechcraft Type 65 Queen Air). Their technique tracks visual markers on the wing through stereo cameras in the cabin. An interesting outcome of this work is the automatic calibration routines necessary to overcome distortions due to cabin

deformation (and thus modification of the camera-window optical system characteristics) during altitude changes. Furthermore, adverse turbulent conditions could induce vibrations that misplace camera orientation. Reference [7] proposes a technique to auto-calibrate the extrinsic camera setup parameters through Image Pattern Correlation Techniques (IPCT), while Ref. [8] pursues the same objective using coded targets instead.

With the advent of small Unmanned Aerial Vehicles (UAVs), the challenges and nuances of wing deformation measurements and techniques have evolved [5]. These include needing lightweight and compact sensors, ensuring energy efficiency, and mitigating challenges posed by diverse operational environments. Additionally, for VFA-like UAVs, the deformation information is required during flight and adds critical real-time and bandwidth requirements. While post-flight photogrammetric analyses are standard in flight testing in the industry, Ref. [6] innovates in proposing modifications in traditional Wind Tunnel Videogrammetric Model Deformation (VMD) measurement techniques to allow for real-time usage in an F/A-18 research aircraft. The pursuit of an online wing shape estimation technique is not entirely new, and dates back to DeAngelis in Ref. [9], who attempted to obtain an analog electro-optical solution to the problem.

An alternative approach to in-flight wing shape estimation uses extended Kalman Filter (EKF) techniques, which attempt to improve estimation precision through data fusion of complementary sensors and information about the system dynamics. In particular, Ref. [10] exploits strain sensor data and the system dynamics model to estimate wing shape displacements dynamically. Additional studies [11–13] propose using computer vision in tandem with strain measurement data. Alternatively, Refs. [11, 12] suggest using Inertial Measurement Units (IMUs), computer vision, and the system dynamics model for EKF-based data fusion. Similarly, Ref. [14] exploits accelerometers, Fiber Optic Strain Sensors (FOSS), and plant information in a linear Kalman filter parametrized to small linear displacements. At the same time, Ref. [15] uses rate gyros, accelerometers, strain gauges, and information on strain-displacement mode shapes to perform flight path reconstruction with an aircraft modal amplitudes and velocities extension. All the works mentioned above require a structural aeroelastic model, which is aircraft-dependent and often challenging to accurately describe its uncertainties through the EKF covariances model. To circumvent this issue, Ref. [17] proposes a standalone camera method that estimates plant parameters amongst structural modal amplitude states through an EKF. The Machine Learning (ML) community is also contributing to this problem. In particular, Ref. [16] compares EKF against Neural Network approaches for wing estimation data fusion.

Finally, the literature is starting to see the first works exploring wing shape estimators in a closed control loop. In particular, Ref. [18] explores the traditional Linear Quadratic Gaussian method of coupling linear optimal control with optimal estimation. The method's robustness is questioned in the paper and calls for Loop Recovery techniques. In this context, Ref. [1] proposes an EKF-based method that exploits rate gyro and computer vision data to estimate large and geometrically nonlinear wing deflections without requiring knowledge of strain-displacement curves or specific aircraft dynamic models, capable of running in real-time with high bandwidth frequency response. The present work continues exploring this technique through real-world data in a controlled experiment in a motion capture room with a mockup wing.

This paper is structured as follows. Section 2 presents the proposed hardware avionics and experimental setup for assessing the technique's viability given real-world data. Section 3 revisits the algorithm and describes its implementation in this work's flexible wing mockup. Section 4 displays the experimental results with our experience feedback and recommendations. We close the paper with our main findings on Sec. 5.

2 Wing Shape Estimator Avionics

We manufactured a flexible wing mockup, including its structure and electronics, to study the wing shape estimation algorithm theoretically presented in Ref. [1]. The setup consists of a high-aspect-ratio mockup wing, i.e., a highly flexible beam (see Fig. 1a), with a square-rod handle at the tip for applying point loads. This wing contains two electronic pods, each featuring a mockup airfoil with a chord length of 14 cm and an IMU. Each station's leading and trailing edges have two Light-Emitting Diodes (LEDs) as visual markers for Computer Vision feature tracking purposes. Additionally, a tiltable sighting device at the wing root points toward the visual markers. Finally, this experiment was conducted in a motion capture (mocap) room for ground truth availability.

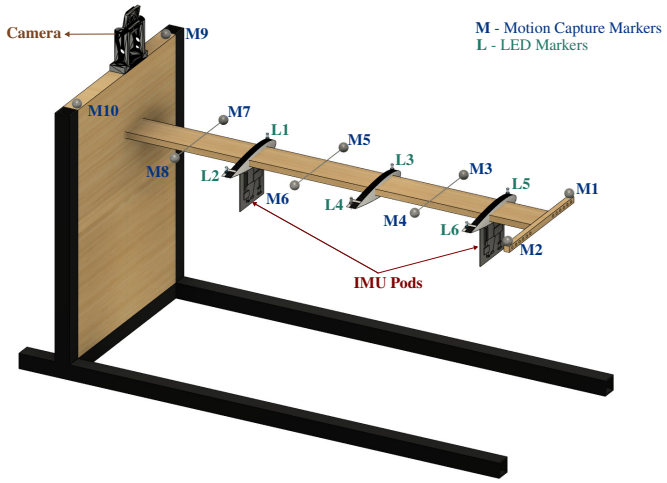

(a) Flexible wing mockup diagram.

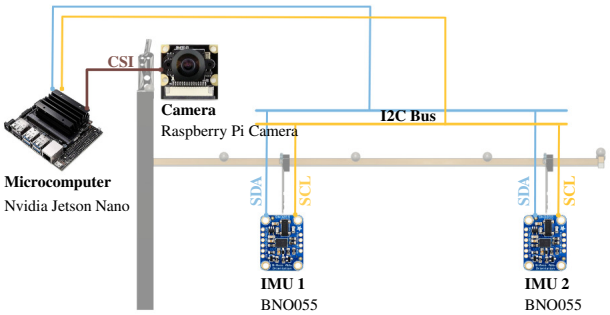

(b) Mockup electronics modules interrelationship.

Although the IMUs, namely Micro Electro-Mechanical System (MEMS) BNO055 modules, provide angular velocity, specific force, and magnetic field measurements at 100Hz, our current algorithm exploits solely the rate gyro outputs (see Sec. 3). Table 1 specifies the sensor chosen rate gyro configuration.

Parameters	Value
Power Mode	NORMAL
Range	$2000°s^{-1}$
Bandwidth	32 Hz
Resolution	16 bits
Sampling Rate	100 Hz

Table 1 Rate Gyro Sensor Configuration.

As a first investigation, we target offline wing shape computation in this work, but our long-term research goal is to obtain a real-time system. Therefore, the control design requirement of real-time estimation imposes low-latency computer vision tracking calculations. In this context, we installed the Nvidia Jetson Nano Single Board Computer (SBC), which includes a Graphics Processing Unit (GPU) that allows for parallel computation and is suitable for low-latency computer vision applications. Furthermore, the suite of available Nvidia CUDA software for target tracking already answers our requirements. It can be readily integrated into our code, with minor overhead due to CPU/GPU memory buffer exchanges.

Each node is equipped with a Printed Circuit Board (PCB) integrated with an IMU sensor and an L7805 linear voltage regulator. Figure 1b provides a schematic representation of the logical connections between the electronic components. Notice that a CSI-interface camera was chosen to avoid the buffering latencies in USB 2.0 interfaces. While USB 3.0 is available in our SBC and provides similar performance

compared to CSI, we avoided that option since our group had previous difficulties with Global Navigation Satellite System (GNSS) receivers interference from USB 3.0 devices.

Finally, our I2C bus for IMUs/SBC communications is temporary. The flyable version of this system includes a CAN bus instead since I2C is unreliable in noisy environments (e.g., an aircraft with electrical motors) for the typical distances of a drone wingspan (we target 6 m).

3 Methodology

This section summarizes previous theoretical work [1] that supports the present flexible wing mockup experiment and applies it to the current setup containing two rate gyro sensors and one camera.

3.1 Wing Deformation Parametrization

Consider an aircraft equipped with M rate gyros distributed along its right wing (see Fig. 2). The structural deflection is modeled by defining a Deformation Reference Line (DRL) fixed to the wing structure (see Fig. 2) passing through all inertial sensors (we assume they're aligned). The application of a vertical load at the wing tip produces a deformation with local anhedral angle ($\phi(s,t)$) with respect to the aircraft body coordinate frame as depicted in Fig. 3. Therefore, we parametrize bending deformations through $\phi(s,t)$, allowing for significant and geometrically nonlinear deformations.

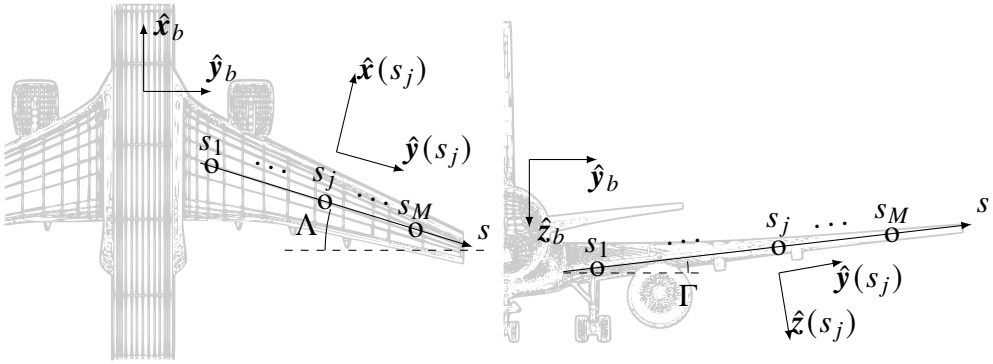

Fig. 2 Rate gyros placement and deformation reference line s definition. (Adapted from Ref. [1].)

Furthermore, we approximate the infinite-dimensional description $\phi(s,t)$ through a finite sum of $N < +\infty$ mode shapes $\tilde{\phi}_i(s)$ according to

$$\phi(s,t) = \sum_{i=1}^{N} \tilde{\phi}_i(s)\phi_i(t) \tag{1}$$

where $\phi_i(t)$ are the respective mode amplitudes. The proposed estimator problem is to estimate $\phi_i(t)$ for $1 \leq i \leq N$ through rate gyro and camera data. A similar description applies to the twist deformation $\theta(s,t)$.

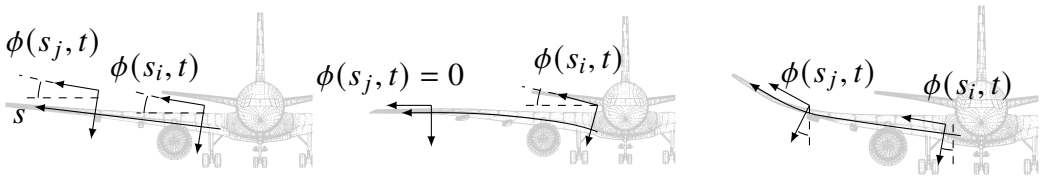

Fig. 3 Deformation examples. (Adapted from Ref. [1].)

3.2 Standalone Rate Gyro Wing Shape Estimation (RG-WSE)

The previously developed technique [1] approaches the problem through the lens of inertial navigation, where a standalone inertial-sensor-based algorithm produces a high-bandwidth estimation solution while its resulting long-term estimation error divergence is settled through additional aiding sensors. This section revisits the standalone inertial algorithm component and fits it to the parameters of the proposed wing mockup.

Application of Eq. 1 to our wing mockup parameters yields

$$\phi(s_j,t) = \tilde{\phi}_1(s_j)\phi_1(t) \quad \text{for} \quad j = 1,2 \tag{2}$$

and

$$\theta(s_j,t) = \tilde{\theta}_1(s_j)\theta_1(t) \quad \text{for} \quad j = 1,2 \tag{3}$$

where s_1 and s_2 are the arclength locations of the two rate gyros, and, since this is the first attempt to apply this particular technique in an experimental setup, we decided to simplify our description to one mode shape for each degree of freedom (e.g., bending and twist).

Accordingly, rate gyro local angular velocities translate to local angle derivatives according to

$$\frac{\partial}{\partial t}\begin{pmatrix}\phi(s_j,t)\\ \theta(s_j,t)\end{pmatrix} = = \underbrace{\begin{bmatrix}1 & \sin\phi(s_j,t)\tan\theta(s_j,t) & \cos\phi(s_j,t)\tan\theta(s_j,t)\\ 0 & \cos\phi(s_j,t) & -\sin\phi(s_j,t)\end{bmatrix}}_{H\left(\phi(s_j,t),\theta(s_j,t)\right)}\begin{pmatrix}P_j(t)\\ Q_j(t)\\ R_j(t)\end{pmatrix} \tag{4}$$

where each rate gyro angular velocity output is modeled by

$$\begin{pmatrix}\hat{P}_j\\ \hat{Q}_j\\ \hat{R}_j\end{pmatrix} = \begin{pmatrix}P_j\\ Q_j\\ R_j\end{pmatrix} + \boldsymbol{\varepsilon}_j + \boldsymbol{w}_j^{(g)} \tag{5}$$

where $\boldsymbol{\varepsilon}_j$ and $\boldsymbol{w}_j^{(g)}$ are, respectively, j^{th} rate gyro's drift and noise. Additionally, $\boldsymbol{\omega}_j = \left(P_j, Q_j, R_j\right)^T$ and $\hat{\boldsymbol{\omega}}_j = \left(\hat{P}_j, \hat{Q}_j, \hat{R}_j\right)^T$ denote, ground truth and measured angular velocities described in the j^{th} rate gyro local frame $\{\hat{\boldsymbol{x}}(s), \hat{\boldsymbol{y}}(s), \hat{\boldsymbol{z}}(s)\}$, respectively. Although the technique allows for rate gyro drift estimation, we will consider in this work $\boldsymbol{\varepsilon}_j = 0$.

If we denote the first and second rows of H in Eq. 4 by $\boldsymbol{H}_\phi(s_j,t)$ and $\boldsymbol{H}_\theta(s_j,t)$, respectively, and differentiate Eqs. 2 and 3, we write

$$\begin{pmatrix}\boldsymbol{H}_\phi^T(s_1,t)\boldsymbol{\omega}_1\\ \boldsymbol{H}_\phi^T(s_2,t)\boldsymbol{\omega}_2\end{pmatrix} = \underbrace{\begin{bmatrix}\tilde{\phi}_1(s_1)\\ \tilde{\phi}_1(s_2)\end{bmatrix}}_{\Phi}\dot{\phi}_1 \quad \text{and} \quad \begin{pmatrix}\boldsymbol{H}_\theta^T(s_1,t)\boldsymbol{\omega}_1\\ \boldsymbol{H}_\theta^T(s_2,t)\boldsymbol{\omega}_2\end{pmatrix} = \underbrace{\begin{bmatrix}\tilde{\theta}_1(s_1)\\ \tilde{\theta}_1(s_2)\end{bmatrix}}_{\Theta}\dot{\theta}_1. \tag{6}$$

The Standalone Rate Gyro Wing Shape Estimation (RG-WSE) algorithm is then obtained through integration of the least squares solutions of the above equations. That is,

$$\dot{\phi}_1 = (\Phi^T\Phi)^{-1}\Phi^T\begin{pmatrix}H_\phi^T(s_1,t)\boldsymbol{\omega}_1\\ H_\phi^T(s_2,t)\boldsymbol{\omega}_2\end{pmatrix} \quad \text{and} \quad \dot{\theta}_1 = (\Theta^T\Theta)^{-1}\Theta^T\begin{pmatrix}H_\theta^T(s_1,t)\boldsymbol{\omega}_1\\ H_\theta^T(s_2,t)\boldsymbol{\omega}_2\end{pmatrix}. \tag{7}$$

Additionally, in state-space representation, Eq. 7 can be written as $\dot{\boldsymbol{x}} = \varphi(\boldsymbol{x}, \boldsymbol{u})$, where $\boldsymbol{x} = (\phi_1, \theta_1)$ and $\boldsymbol{u} = (\omega_1, \omega_2)$. Figure 4 illustrates the algorithm schematically.

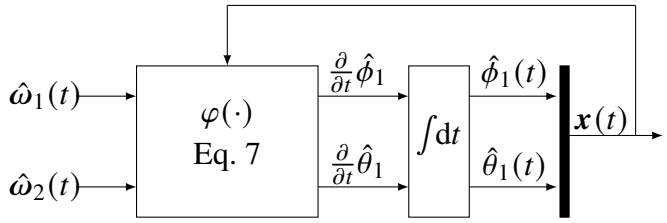

Fig. 4 Schematic of the RG-WSE algorithm. (Adapted from Ref. [1]).

3.3 An RG-WSE Error Model for the EKF

The following describes the RG-WSE error model that implements the Extended Kalman Filter (EKF) Prediction Phase in the following section. Accordingly, the EKF state vector is defined as

$$\boldsymbol{x}_{\text{EKF}} = \begin{pmatrix} \delta\phi_1 & \delta\theta_1 \end{pmatrix}^T \tag{8}$$

where $\delta\theta_1, \delta\phi_1$ represent the error states, given by the difference between true and estimated states. The dynamics of $\boldsymbol{x}_{\text{EKF}}$ is derived by linearizing Eq. 8, such that

$$\dot{\boldsymbol{x}}_{\text{EKF}} = \varphi(\boldsymbol{x}, \boldsymbol{u}) - \varphi(\hat{\boldsymbol{x}}, \hat{\boldsymbol{u}}) \approx \underbrace{\begin{bmatrix} \frac{\partial\varphi}{\partial\phi_1} & \frac{\partial\varphi}{\partial\theta_1} & \frac{\partial\varphi}{\partial\boldsymbol{u}} \end{bmatrix}}_{A} \boldsymbol{x}_{\text{EKF}} + \underbrace{\frac{\partial\varphi}{\partial\boldsymbol{u}}}_{G} \boldsymbol{w}^{(g)} \tag{9}$$

where $\boldsymbol{w}^{(g)}$ aggregates all the sensor noise vectors, i.e., $\boldsymbol{w}^{(g)} = (\boldsymbol{w}_1^{(g)}, \boldsymbol{w}_2^{(g)})$, and all the Jacobians are evaluated at $(\hat{\boldsymbol{x}}, \hat{\boldsymbol{u}})$, obtained in practice during the experiment numerically through the Complex Step linearization technique.

3.4 Camera-Aided Rate Gyro Wing Shape Estimation (CRG-WSE)

In this section, we bound the RG-WSE estimation errors by adding camera measurements through an EKF. To implement the discrete-time EKF, the continuous-time model is discretized through finite differences to yield

$$\boldsymbol{x}_{EKF}(t_k) \approx \boldsymbol{x}_{EKF}(t_{k-1}) + \dot{\boldsymbol{x}}_{EKF}\Delta t = \underbrace{(A\Delta t + I)}_{F_k} \boldsymbol{x}_{EKF}(t_{k-1}) + G_k \partial\boldsymbol{w}^{(g)} \tag{10}$$

where $\partial\boldsymbol{w}^{(g)}$ is the discrete-time white noise equivalent of $\boldsymbol{w}^{(g)}$. The statistics of $\partial\boldsymbol{w}^{(g)}$ should conform to rate gyro manufacturer specifications.

3.4.1 Prediction Step (RG-WSE)

The state prediction $\hat{\boldsymbol{x}}_{k|k-1}$ and error covariance prediction $P_{k|k-1}$ are given by

$$\begin{aligned} \hat{\boldsymbol{x}}_{k|k-1} &= F_k \hat{\boldsymbol{x}}_{k-1|k-1} \\ P_{k|k-1} &= F_k P_{k-1|k-1} F_k^T + G_k Q_k G_k^T \end{aligned} \tag{11}$$

where Q_k, $P_{k|k}$ and $P_{k|k-1}$ are the covariance of the rate gyros noise, the *a posteriori* error covariance matrix, and the *a priori* error covariance, respectively.

3.4.2 Update Step (Computer Vision)

The proposed rate gyro and sighting device data fusion technique is based on tracking fixed visual markers M_k on the wing; each with *a priori* known wing location (s_k, x_k, z_k). For each marker M_k, $k = 1..6$, its position with respect to the wing root camera C, denoted by $\boldsymbol{p}^{k/c} \in \mathbb{R}^3$, is described in the C camera coordinate frame as

$$\boldsymbol{p}^{k/c} = -D_c^f \boldsymbol{r}_f^C + D_c^f \boldsymbol{r}_f(s_k, t) + D_c^f D\left(\phi(s_k, t), \theta(s_k, t), \psi(s_k, t)\right)^T \begin{pmatrix} x_k \\ 0 \\ z_k \end{pmatrix} \tag{12}$$

where D_c^f and $\boldsymbol{r}_f^C$, denote the direction cosine matrix from body frame to camera C frame, and camera position with respect to wing root in body frame, respectively (see Fig. 5). The camera is assumed fixed in body frame and thus D_c^f is constant. Hence the camera measurement $\boldsymbol{z}^{k/c} \in \mathbb{R}^2$ in pixels is given by

$$\boldsymbol{z}^{k/c} = \Pi \frac{f \boldsymbol{p}^{k/c}}{\begin{bmatrix} 1 & 0 & 0 \end{bmatrix} \boldsymbol{p}^{k/c}} \quad \text{where} \quad \Pi = \begin{bmatrix} 0 & 1 & 0 \\ 0 & 0 & 1 \end{bmatrix} \tag{13}$$

and $f \in \mathbb{R}$ is the focal length in pixels.

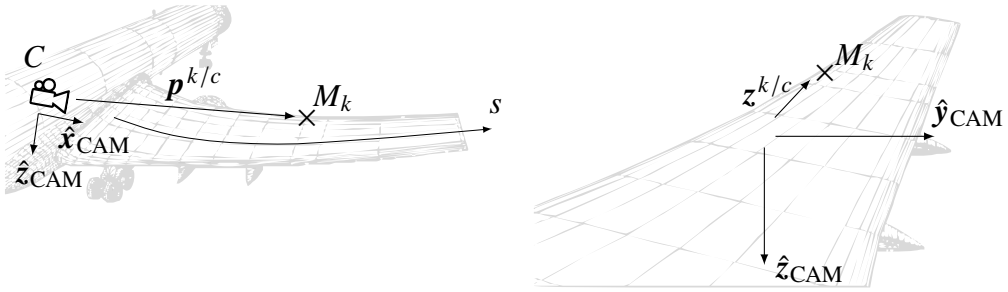

a) Camera axis definition and symbols. b) Camera view.

Fig. 5 Camera-related symbols and frame definitions. (Adapted from Ref. [1].)

Given these assumptions, $\boldsymbol{z}^{k/c}$ depends exclusively on modal amplitudes ϕ_1 and θ_1. Therefore, $\boldsymbol{z}^{k/c}$ linearization yields

$$\underbrace{\boldsymbol{z}^{k/c}(\phi_1, \theta_1) - \boldsymbol{z}^{k/c}(\hat{\phi}_1, \hat{\theta}_1)}_{\triangleq \Delta \boldsymbol{z}^{k/c}} = \frac{\partial \boldsymbol{z}}{\partial \phi_1}^{k/c} \delta\phi_1 + \frac{\partial \boldsymbol{z}}{\partial \theta_1}^{k/c} \delta\theta_1 \tag{14}$$

Consequently, an appropriate model for an observation equation is given by

$$\Delta \boldsymbol{z}^{k/c} = \underbrace{\begin{bmatrix} \frac{\partial \boldsymbol{z}}{\partial \phi_1}^{k/c} & \frac{\partial \boldsymbol{z}}{\partial \theta_1}^{k/c} \end{bmatrix}}_{H^{k/c}} \boldsymbol{x}_{EKF} + \boldsymbol{w}_{CAM}^{k/c} \tag{15}$$

where $\boldsymbol{w}_{CAM}^{k/c} \in \mathbb{R}^2$ is additive white Gaussian noise with statistics depending on camera quality, tracking algorithm performance and marker–camera positioning. The Kalman gain, updated state, and updated

error covariance are computed through the classical Kalman filter formulae :

$$
\begin{aligned}
\boldsymbol{y}_k &= \Delta \boldsymbol{z}^{k/c} - H^{k/c}\hat{\boldsymbol{x}}_{k|k-1} \\
S_k &= H^{k/c} P_{k|k-1} (H^{k/c})^T + R_k \\
K_k &= P_{k|k-1} (H^{k/c})^T S_k^{-1} \\
\hat{\boldsymbol{x}}_{k|k} &= \hat{\boldsymbol{x}}_{k|k-1} + K_k \boldsymbol{y}_k \\
P_{k_k} &= (I - K_k H^{k/c}) P_{k|k-1}
\end{aligned}
\tag{16}
$$

where $R_k = E[\boldsymbol{w}_{CAM}^{k/c} (\boldsymbol{w}_{CAM}^{k/c})^T]$ is the measurement noise covariance, and the mean of the measurement noise is assumed to be zero. Figure 6 illustrates the entire algorithm.

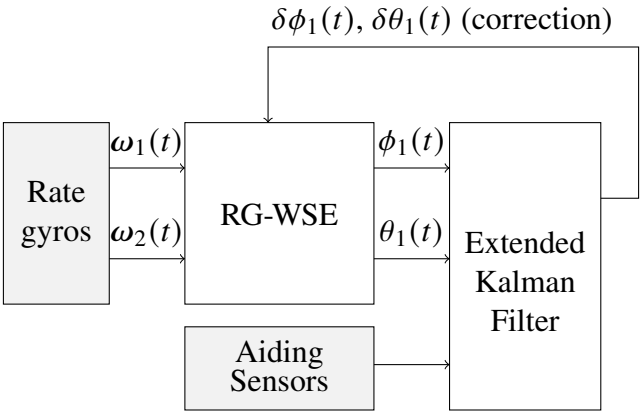

Fig. 6 Aided inertial wing shape estimator overall architecture. (Adapted from Ref. [1].)

3.5 Computer Vision Tracking

For Computer Vision purposes, we exploit OpenCV, a popular opensource project containing a library of eight tracking algorithms (namely, BOOSTING, MIL, KCF, TLD, MEDIANFLOW, GOTURN, MOSSE, and CSRT) which were assessed according to the following quantitative and qualitative performance criteria: computational tracking time, achievable frames per second (FPS), occlusion robustness, out-of-view markers tracking recovery, marker agile motion tracking and invariance to illumination changes (see Table 2). After analysis, we chose the *Kernalized Correlation Filter* (KCF) and the *Channel and Spatial Reliability Tracker* (CSRT) [19] for our experiments. While CSRT and KCF fill all requirements, CSRT displayed more robustness in scenarios where regions of interest (ROIs) are subject to high-frequency and indeterministic motion. Hence, the CSRT algorithm will be employed for the camera-aided component of the state estimation procedure, even if KCF shows higher FPS. This tradeoff will have to be further investigated for future real-time experiments.

3.6 Intrinsic and Extrinsic Camera Parameters Calibration

The EKF camera model relies on knowledge of the following intrinsic/extrinsic camera setup parameters: the position of the camera with respect to the wing root $\boldsymbol{r}_f^C$, the camera tilt angle θ_c, and the camera focal length f. While the extrinsic parameters can be directly measured using rulers and protractors, the intrinsic focal length calls for a camera calibration procedure, which has been conducted through standard OpenCV camera calibration routines. In particular, a 6x8 chessboard image in various configurations within the camera's field of view were processed to yield the intrinsic camera matrix and the distortion coefficients, including the focal length.

However, while validating the EKF camera model by projecting the known mocap markers' positions on the predicted camera plane using the camera estimated parameters, we had discrepant results between

Algorithm	FPS	Occlusion	Out-of-view	Agile Motion	Illumination Changes
BOOSTING	15	NO	NO	NO	NO
MIL	4	NO	YES	NO	NO
KCF	50	YES	YES	YES	YES
TLD	6	NO	NO	YES	NO
MEDIANFLOW	50	YES	NO	YES	NO
GOTURN	150	NO	NO	NO	NO
MOSSE	300	NO	NO	YES	NO
CSRT	10	YES	YES	YES	YES

Table 2 Computer Vision tracking algorithms comparison.

the predicted and actual markers' positions on the video frame. This signaled that the precision of our camera parameters needed improvement.

Therefore, an auto-calibration optimization algorithm was developed to improve the camera parameters' precision. In particular, the developed tool minimizes a cost function that adds up all distances between predicted and actual markers' positions in the image frame (i.e., in pixels) for one chosen instant of time by looking into the space of possible $\boldsymbol{r}_f^C$, θ_c and f. We found that while the tilt orientation saw a substantial re-adjustment, there was no visible change in the camera coordinates $\boldsymbol{r}_f^C$.

3.7 Determination of Mode Shapes

The CRG-WSE algorithm requires the definition of first wing mode shapes $\tilde{\phi}_1(s)$ and $\tilde{\theta}_1(s)$. These were computed using a snapshot of the wing mockup subjected to a point load at the tip (see Fig. 7), in contrast to the commonplace eigenvector computation of a linearized structural dynamics model. This choice is justified by the fact that our experiment is conducted under quasi-static conditions over a large wing deflection envelope instead of small disturbances in the neighborhood of a trimmed condition.

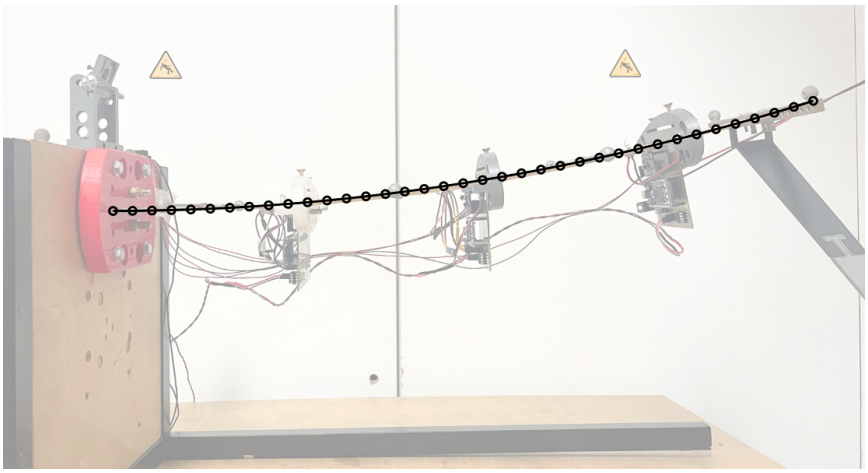

Fig. 7 Computation of selected mode shape $\tilde{\phi}(s) = 0.3776 \cdot s$.

4 Experiment and Results

The experiment is conducted in a motion capture facility, which logs at 50 Hz the position of ten installed markers (see Sec. 2) up to millimetric precision and thus is used as ground truth. We apply

Fig. 8 Experimental setup and manual loads application method.

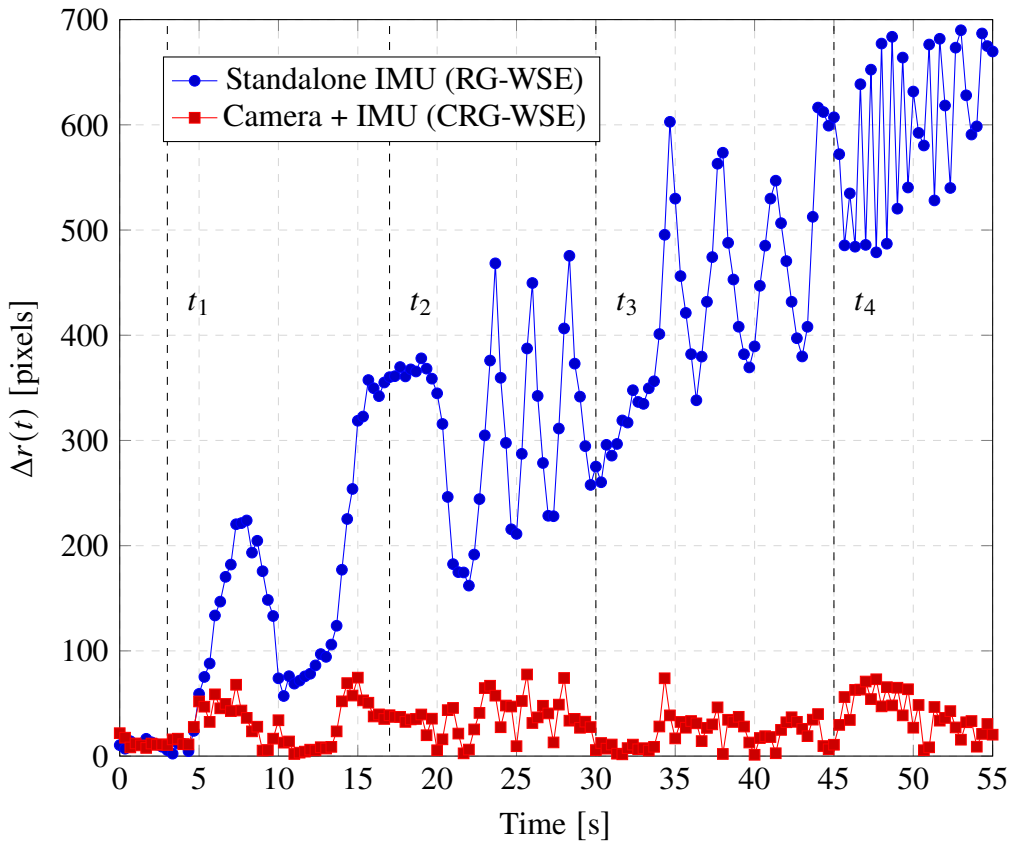

Fig. 9 Motion capture markers estimated position errors in the camera frame $|\Delta \boldsymbol{r}(t)|$ for the RG-WSE and CRG-WSE algorithms. Figure 10 illustrates the visual outcome of selected time instants t_i, $i = 1..4$, for a visual interpretation of the magnitudes of the performance index $|\Delta \boldsymbol{r}(t)|$.

large and small amplitude pure-bending deflections at various frequencies through a string fastened at the center of the square-rod handle at the beam tip (see Fig. 8). During the experiment, the SBC records the wing root camera stream and simultaneously logs the rate-gyro angular rates in the local DRL frame

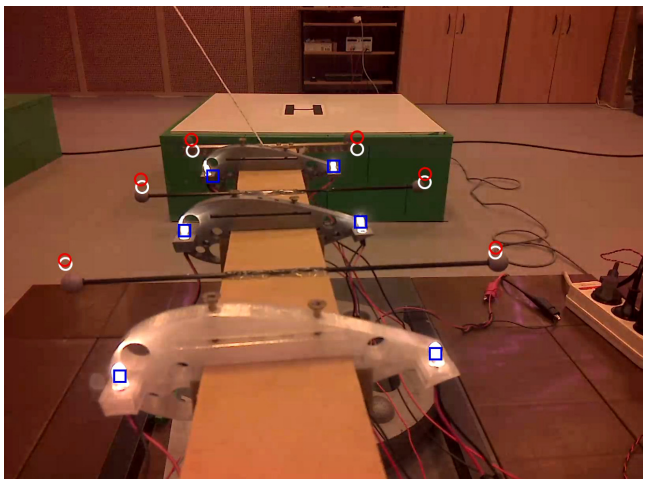

(a) Camera output at t_1.

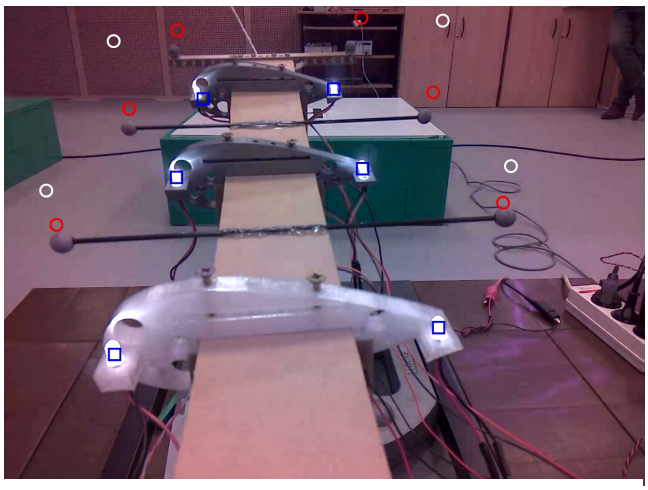

(b) Camera output at t_2.

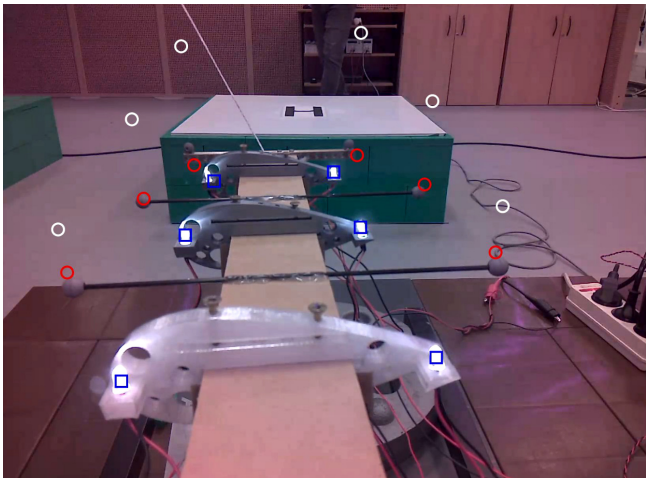

(c) Camera output at t_3.

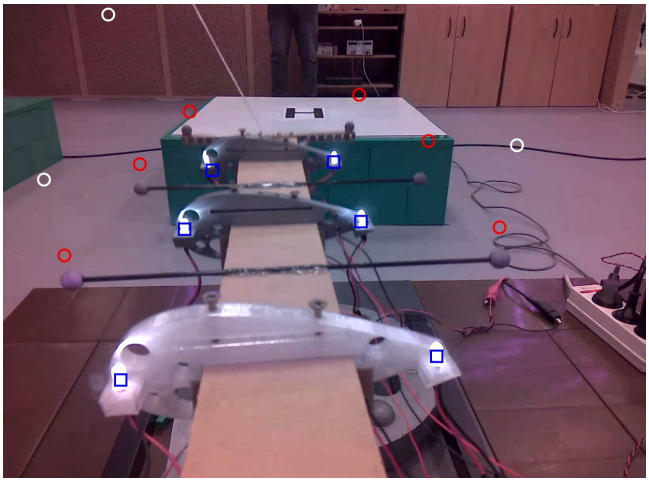

(d) Camera output at t_4.

Fig. 10 Illustration of the visual outcome of selected time instants t_i, $i = 1..4$, for a visual interpretation of the magnitudes of the performance index $|\Delta r(t)|$. See Fig. 9 for the performance indexes outcome in time. Blue squares denote the output of the computer vision tracking algorithm, while white circles denote RG-WSE standalone IMU algorithm output, and red circles denote the CRG-WSE EKF-based algorithm outcome.

of reference from the two IMUs. All RG-WSE and CRG-WSE computations are performed offline (after calibration of intrinsic and extrinsic camera parameters according to Sec. 3.6) and compared against the mocap ground truth.

We define the figure of merit for the error $\Delta r(t)$ as

$$\Delta r(t) = \sum_{\text{visible markers}} \frac{|\hat{\boldsymbol{r}}_i(t) - \boldsymbol{r}_i^*(t)|}{N_{\text{visible markers}}} \tag{17}$$

where $\hat{\boldsymbol{r}}_i(t)$ is the estimated marker position from either the RG-WSE or the CRG-WSE algorithms projected in the camera plane and $\boldsymbol{r}_i^*(t)$ the true marker position as measured by the motion capture facility, also projected in the camera frame. This error is used as a performance index to compare the results between the above two methodologies. These results are depicted in Fig. 9, and show that standalone IMU estimation yields error divergence, as predicted by previous work [1]. Additionally, incorporating the camera data reduces and bounds the errors.

The experiment consisted of a frequency sweep in bending, which is visible in Fig. 9 through the increasing frequency of the error signal in the Standalone IMU (RG-WSE) curve. Additionally, the increase in frequency (inside the bandwidth tested in this experiment) does not worsen the estimation in both methods. In particular, the CRG-WSE method yields a constant error bound throughout the frequency sweep. On the other hand, the RG-WSE shows a constant error rate independent of vibration frequency. Finally, while we did not see error amplification in CRG-WSE in our test frequency band, we plan to reproduce this exercise in higher frequencies to estimate better the filter bandwidth and associated trade-offs (e.g., noise disturbance and robustness in a control loop).

In time instant t_1, during initialization of the system, when the wing is at rest, we have our best performance indexes $|\Delta \boldsymbol{r}(t)|$, which are reflected in Fig. 10 by the observed superposition of mocap markers (i.e., solid gray spherical features at each black rod ends) and RG-WSE and CRG-WSE predictions of the position of same markers, respectively given by the white and red circles. During consequent time instants, we observe RG-WSE error divergence through the increasing mismatch between mocap markers' positions and their respective RG-WSE predictions (white circles). On the other hand, we observe CRG-WSE error boundness through the comparatively minor position mismatches, which are not increasing with time.

5 Conclusion

This paper exemplifies a wing shape estimation methodology through an experimental mockup. We confirmed previous theoretical predictions of rapidly unstable errors if only IMUs are employed and stable estimation if camera data is added. Large, geometrically nonlinear, and varying-frequency deflections were tested, and the results show encouraging results for upcoming work on the real-time implementation. We are confident that computer vision should not be a problem given our obtained FPS. On the other hand, the fact that the angle-based deformation description requires an integration process at every sample time instant to obtain wing displacements should be further investigated.

References

[1] L. R. Lustosa, I. Kolmanovsky, C. E. S. Cesnik, and F. Vetrano, "Aided inertial estimation of wing shape"," *Journal of Guidance, Control, and Dynamics*, vol. 44, no. 2, pp. 210–219, 2021. DOI: 10.2514/1.G005368

[2] Z. Ma and X. Chen,"Fiber Bragg gratings sensors for aircraft wing shape measurement: Recent applications and technical analysis," *Sensors*, vol. 19, no. 1, pp. 55, 2018. DOI: 10.3390/s19010055

[3] R. Tagai, K. Nakakita, M. Kurita, and T. Nakajima, "Wing Deformation Measurement as Bases for In-Flight Aerodynamics," In *AIAA Flight Testing Conference*, pp. 3355, 2016. DOI: 10.2514/6.2016-3355.

[4] M. Kurita, S. Koike, K. Nakakita, and K. Masui, "In-flight wing deformation measurement," In *51st AIAA Aerospace Sciences Meeting including the New Horizons Forum and Aerospace Exposition*, p. 967, 2013.

[5] Z. Y. Pang, C. E. Cesnik, and E. M. Atkins, "In-flight wing deformation measurement system for small unmanned aerial vehicles," In *55th AIAA/ASMe/ASCE/AHS/SC Structures, Structural Dynamics, and Materials Conference*, pp. 0330, 2014. DOI: 10.2514/6.2014-0330

[6] A. W. Burner, W. A. Lokos, and D. A. Barrows, "In-flight aeroelastic measurement technique development," In *Optical diagnostics for fluids, solids, and combustion II*, vol. 5191, pp. 186–199, 2003, organization: SPIE. DOI: 10.1117/12.504157.

[7] T. Kirmse, "Recalibration of a stereoscopic camera system for in-flight wing deformation measurements," *Measurement Science and Technology*, vol. 27, no. 5, pp. 054001, 2016. DOI: 10.1088/0957-0233/27/5/054001

[8] Y. Liu, Z. Ge, Y. Yuan, X. Su, X. Guo, T. Suo, and Q. Yu, "Wing deformation measurement using the stereo-vision methods in the presence of camera movements," *Aerospace Science and Technology*, vol. 119, p. 107161, 2021. DOI: 10.1016/j.ast.2021.107161

[9] V. M. DeAngelis, "In-flight deflection measurement of the HiMAT aeroelastically tailored wing," *Journal of Aircraft*, vol. 19, no. 12, pp. 1088–1094, 1982. DOI: 10.2514/3.44816

[10] T. Joels and D. E. Raveh, "Wing dynamic shape-sensing from fiber-optic strain data using the Kalman state estimator," *Aerospace Science and Technology*, vol. 137, p. 108286, 2023. DOI: 10.1016/j.ast.2023.108286

[11] A. Kotikalpudi, B. P. Danowsky, D. K. Schmidt, C. D. Regan, and A. Gupta, "Real-time shape estimation for a small flexible flying-wing aircraft," In *AIAA Scitech 2019 Forum*, p. 1818, 2019. DOI: 10.2514/6.2019-1818

[12] A. Kotikalpudi, D. K. Schmidt, C. D. Regan, and P. J. Seiler, "Real-time shape estimation for flexible unmanned air vehicle via Kalman filtering," In *AIAA Scitech 2020 Forum*, p. 1267, 2020. DOI: 10.2514/6.2020-1267

[13] T. Joels and D. E. Raveh, "Dynamic Shape Sensing of the A3TB Wind Tunnel Model Using Fiber Optics Strain Data and the Kalman State Estimator," In *AIAA SCITECH 2023 Forum*, p. 1310, 2023. DOI: 10.2514/6.2023-1310

[14] J. A. Grauer, "Method for Real-Time State Estimation of Structural Modes for an Aeroelastic Wind Tunnel Model," In *AIAA Scitech 2021 Forum*, p. 1643, 2021. DOI: 10.2514/6.2021-1643

[15] A. Jurisson, B. Eussen, C. C. de Visser, and R. De Breuker, "Flight path reconstruction filter extension for tracking flexible aircraft modal amplitudes and velocities," In *AIAA SCITECH 2023 Forum*, p. 0626, 2023. DOI: 10.2514/6.2023-0626

[16] B. Z. Hadlaczky, N. Friedman, B. Takarics, and B. Vanek, "Comparison of EKF and Neural Network based wing shape estimation of a flexible wing demonstrator," *International Forum on Aeroelasticity and Structural Dynamics (IFASD) 2022*, 2022.

[17] T. Mkhoyan, C. C. de Visser, and R. De Breuker, "Adaptive state estimation and real-time tracking of aeroelastic wings with augmented Kalman filter and kernelized correlation filter," In *AIAA Scitech 2021 Forum*, p. 0666, 2021. DOI: 10.2514/6.2021-0666

[18] S. Duessler, T. Mylvaganam, and R. Palacios, "LQG-based Gust Load Alleviation Systems for Very Flexible Aircraft," In *AIAA SCITECH 2023 Forum*, p. 2571, 2023. DOI: 10.2514/6.2023-2571

[19] O. Haggui, M. A. Tchalim, and B. Magnier, "A comparison of OpenCV algorithms for human tracking with a moving perspective camera," In *2021 9th European Workshop on Visual Information Processing (EUVIP)*, pp. 1-6, June 2021, IEEE.